

Rapid search for massive black hole binary coalescences using deep learning

Wen-Hong Ruan,^{1,2,*} He Wang,^{1,†} Chang Liu,^{3,2,‡} and Zong-Kuan Guo^{1,2,3,§}

¹*CAS Key Laboratory of Theoretical Physics, Institute of Theoretical Physics,
Chinese Academy of Sciences, Beijing 100190, China*

²*School of Physical Sciences, University of Chinese Academy of Sciences, No.19A Yuquan Road, Beijing 100049, China*

³*School of Fundamental Physics and Mathematical Sciences, Hangzhou Institute for Advanced Study,
University of Chinese Academy of Sciences, Hangzhou 310024, China*

The coalescences of massive black hole binaries (MBHBs) are one of the main targets of space-based gravitational wave observatories. Such gravitational wave sources are expected to be accompanied by electromagnetic emission. Low latency time of gravitational wave searches and accurate sky localization are keys in triggering successful follow-up observations on the electromagnetic counterparts. Here we present a deep learning method for the first time to rapidly search for MBHB signals in the strain data. Our model is capable to process 1-year of data in just several seconds, identifying all MBHB coalescences with no false alarms. We test the performance of our model on the simulated data from the LISA data challenge. We demonstrate that the model shows a robust resistance for a wide range of generalization for MBHB signals. This method is supposed to be an effective approach, which combined the advances of artificial intelligence to open a new pathway for space-based gravitational wave observations.

I. INTRODUCTION

On September 14, 2019, a transient gravitational wave (GW) signal from a compact binary coalescence (CBC) was observed by the Laser Interferometer Gravitational-Wave Observatory (LIGO), which is the first directly detection of GWs [1]. Since then, a number of CBC events [2, 3] have been detected by Advanced LIGO and Advanced Virgo. In the third Gravitational-wave Transient Catalog [4], they have confidently found a total of 90 CBC candidates in the first three observing runs. GW observations have opened a completely new window for astrophysical processes and fundamental physics.

The GW signals detected by LIGO and Virgo mainly come from the coalescence of stellar mass black hole binaries. In addition, it is known that massive black hole binaries (MBHBs) are also ubiquitous in galaxy centers [5–7]. The Laser Interferometer Space Antenna (LISA), a proposed space-based detector, is able to detect GWs emitted from coalescing MBHBs with total masses of $10^5 M_\odot - 10^8 M_\odot$ [8]. GW observations could improve our understanding of the evolution of galaxies and the Universe. MBHBs may produce detectable electromagnetic emission associated with the final merger. Quickly identifying and localizing MBHB coalescences by GW observations is a key for the detection of electromagnetic counterparts. The multi-messenger observation for MBHB coalescences is much helpful to find out the host galaxy, which provides the prospect for resolving the Hubble tension as standard sirens [9, 10]. However, it has been estimated that the GW signals emitted from tens of millions Galactic binaries [11] will enter the sensitivity band of

LISA. Furthermore, LISA is able to detect a rich source of GWs including the extreme mass ratio inspirals, intermediate mass black hole binaries with total mass between 600 and $10^4 M_\odot$ and stellar mass black hole binaries [8]. More signals like bursts from unknown astrophysical systems and stochastic GW backgrounds from cosmological and astrophysical process may also be present in LISA data. Therefore, LISA data will contain a superposition of GW signals from numerous resolved and unresolved sources, which brings great challenges to extract information of every source individually.

The global fit analysis [12] has been considered for the exploration in a large parameter space of an unknown number of sources with a great computational cost. From another perspective, GWs emitted from coalescing MBHBs can evolve in the LISA band for months or even years, which indicates that they might be overlapping in LISA data. Accordingly, once every MBHB coalescence is found out, the global-fit analysis for these sources just tackles the case with a fixed number of parameters. The data analysis can be employed on a short data segment instead of a long data containing the full signal. In this case, the follow-up parameter estimation is performed rapidly, which is significant to determine the sky location of MBHBs in a short time.

In this paper, we make the first attempt on searching for MBHB coalescences in LISA data using deep learning [13] which has been widely applied in ground-based GW data analysis [14]. Nevertheless, the characteristics of LISA data are much more different from LIGO data. GW signals in LISA data are more complicated due to the modulation by the motion of detectors [15]. Moreover, the application of time-delay interferometry (TDI) technique will further increase the complexity of GW signals [16]. It is worth testing the capability of deep learning on LISA data.

In this work, we construct a matched-filtering convolutional neural network (MFCNN) [17] to distinguish

* ruanwenhong@itp.ac.cn

† hewang@itp.ac.cn

‡ liuchang@ucas.ac.cn

§ guozk@itp.ac.cn

whether there are MBHB mergers in a data segment, which absorbs the advantages of the matched filtering [18] and convolutional neural network (CNN) [19]. The matched filtering method is an optimal algorithm searching for weak signals with known features in noisy data, and it has achieved extraordinary success in ground-based GW detection [20]. The CNN, a class of artificial neural networks in deep learning, has the powerful capability in feature extraction. Nowadays, quantitative works of GW searches by the CNN for ground-based detectors have been conducted by many authors [17, 21–27]. Their works show that the CNN architecture can find GW candidates much more rapidly than the matched filtering method. Here we use the MFCNN to figure out the short data segments containing MBHB mergers. The coalescence time will be limited to a small range and the number of parameters for data analysis can be determined. It greatly reduces the computational cost of parameter estimation and can be regarded as a part of data preprocessing. Our model takes only several seconds to analyze 1-year LISA data. All MBHB coalescences are identified within several days of data with no false alarms. It also shows robustness against the generations of TDI. Although we focus on LISA data in this work, our model is expected to be easily extended to other space-based GW detectors such as Taiji [28].

This paper is organized as follows. In Sec. II, we describe the MFCNN framework that combines the matched filtering method and the CNN. The strategy to search for GW signals in data is described in Sec. III. In Sec. IV, we explain the components and distribution of training datasets. The results of test are shown in Sec. V and finally we give a summary in Sec. VI.

II. MATCHED-FILTERING CONVOLUTIONAL NEURAL NETWORKS

In this section, we present our architecture of the MFCNN combining the matched filtering method and the CNN. The matched filtering plays a vital role in ground-based GW detection based on the existing full waveform template bank. Its search and response to GW signals are limited to the feature of existing complete waveforms. GW signals beyond the template bank cannot be easily detected. For the CNN, as a supervised type of deep learning method, it can learn the universal features automatically from the waveforms. The extracted features associated with GW waveforms form the learnable parameters in a trained CNN model. Based on that, the MFCNN model combines the power of the template matching for weak signals and feature representations with the deep learning method. The generalization ability of the CNN model will help us to discover signals beyond the existing templates.

In practice, the MFCNN model attempts to rewrite the SNR of matched filtering in the frequency domain as convolution operation in the time domain. Traditionally,

the SNR of the matched filter is defined by [29]

$$\rho^2(t) = \frac{|\langle d|h \rangle(t)|^2}{\langle h|h \rangle}, \quad (1a)$$

$$\langle d|h \rangle(t) = 4 \int_0^\infty df \frac{\tilde{d}(f)\tilde{h}^*(f)}{S_n(f)} e^{i2\pi ft}, \quad (1b)$$

$$\langle h|h \rangle = 4 \int_0^\infty df \frac{\tilde{h}(f)\tilde{h}^*(f)}{S_n(f)}, \quad (1c)$$

where d is the strain data, h is a template for the waveform and $S_n(f)$ is the one-sided power spectral density (PSD) of noise. Here $\tilde{a}(f)$ denotes Fourier transform of real-valued time series $a(t)$. Generally, the detection strategy to identify GW candidates involves setting a lower threshold on ρ .

The basic idea of the MFCNN model is to use the prepared waveform templates h as learnable parameters in neural network layers. Practically, the first layer of the neural network we constructed is similar to the matched filtering process. In this layer, the strain data d are whitened as

$$\bar{d}(t) = d(t) * \bar{S}_n(t), \quad (2a)$$

$$\bar{S}_n(t) = \int_{-\infty}^{+\infty} df S_n^{-1/2}(f) e^{i2\pi ft}, \quad (2b)$$

where $a(t) * b(t)$ denotes the convolution of two time series. Then, the convolution $\bar{d}(t) * \bar{h}_i(-t)$ will be calculated in this layer, which is similar to Eq. (1b). The coefficients \bar{h}_i ($i = 1, 2, \dots, N_t$) are fixed and correspond to a whitened theoretical template, which are given by $\bar{h}_i(t) = h_i(t) * \bar{S}_n(t)$. Next, the maximum value of the output will be passed through the rest layers after normalization, and the normalization operation is given by

$$\bar{d}(t) * \bar{h}_i(-t) \longrightarrow \frac{\bar{d}(t) * \bar{h}_i(-t)}{[\bar{h}_i(t) * \bar{h}_i(-t)]|_{t=0}}. \quad (3)$$

Analogous to the convolutional layer, the whitened template \bar{h}_i can be regarded as a convolution kernel that extracts features from the strain data. The rest part of the neural network is the same as the usual CNN network. At last the MFCNN will output the predictions of MBHB signals from a softmax function, which is commonly-used in the CNN. The framework of the MFCNN model is presented in Fig. 1. The architecture will admit some feature structures with respect to a small number of templates which can be recognized by the CNN layers. This can be used to distinguish GW signals from noise.

III. SEARCH STRATEGY

In this section, we develop our conceptual contributions of search strategy for GW signals, namely that (a)

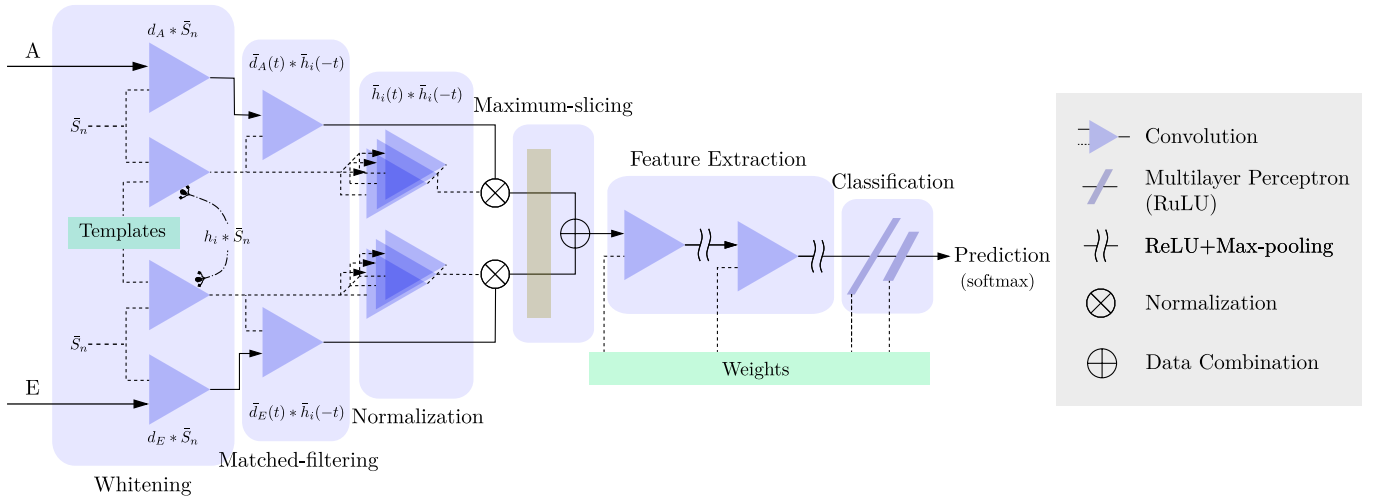


FIG. 1. Framework of the MFCNN used in this work.

probability predictions from any models output with the softmax function are not suited to claim statistically significant detections of GWs, however, (b) they can still be useful statistics for trigger generation. This area of research is especially important for understanding how to identify the temporal location of potential GW signals and diminish the false alarms in streaming data.

Our core argument for claim (a) hinges on the fact that the negative log-likelihood cost function applied on models with the softmax function always strongly penalizes the most active incorrect prediction, and the correct output for the samples with large SNR contributes little to the learnable parameters of model (see Sec. 6.2.2.3 in [13]). Therefore, certain binary classifiers can come up with an effective decision boundary between non-signal-free and signal-free samples. However it performs badly for ranking influential non-signal-free samples, which are not monotonic influential on the SNR or other statistics [17]. As a consequence, the significance level obtained from model prediction with softmax can not be treated as valid ranking statistic to distinguish loud triggers from fainter ones.

To substantiate (b), we highlight that by either “repeated-modeling” or “repeated-sampling” analysis on the short data segment one can provide a search strategy to indicate confidence level and diminish the false alarms. For example, the multi-model stacking ensemble learning for GW detection [30, 31] can combine the output of each independent sub-model to identify GW triggers that pass a given threshold. Intuitively, the probability of misclassification decreases with an increase in the number of sub-models. In addition, a repeated analysis on the target data with a single model is another way to contribute to the significance of candidates with frequentist interpretations. Similar to time-shifted analysis [32] used to create a larger number of data to approximate the background noise, “repeated-sampling” analysis first applied in [17] takes longer data segment as input data and

high overlap with each neighbouring samples to repeatedly estimate the background around the target short data segment. Thus, for a signal hiding somewhere in the streaming data, a simple value comparison of continuous alerts from model prediction can help to detect the trigger and rule out the false positive candidates.

In a real search, we adopt “repeated-sampling” analysis to search for MBHB signals in a very-long-duration data set as shown in Sec. VB. For each input segment of a given streaming data, we choose to overlap segments by 80% and let the MFCNN process. In other words, as we continuously move forward one fifth of the input, an overlapping snippet will appear in five segments and be processed 5 times by our model. Afterwards, we define a local-maximum trigger as 5 (or more than 5) neighbouring segments of same values predicted from the MFCNN that are surrounded by the segments with smaller values. For record purposes, we output the center time of each input segment and the potential coalescence time of MBHB signals.

IV. DATASET

The capabilities of the CNN-based architecture are largely dependent on the construction of training dataset. In this work, training datasets can be divided into two categories, one contains MBHB signals and noise, and the other only contains noise. Note that GW signals from other types of sources are regarded as noise here. We use the IMRPhenomD model [33, 34] to simulate 3,000 waveforms of non-precessing MBHBs at redshift $z = 1, 3, 6, 10, 15$, respectively. In details, we use a logarithmic scaling to sample redshifted total mass $M_z = M(1+z)$ in the range of $(10^{5.4}M_\odot, 10^8M_\odot)$ with steps of 0.013 and mass ratio q is sampled in the range of (1, 15) with steps of 1 ($M = m_1 + m_2$ is the total mass of the two companions). Other parameters are sampled from

Parameter	Description	Prior
i	Inclination relative to line-of-sight	Uniform($0, \pi$)
β	Ecliptic latitude	Uniform($-\frac{\pi}{2}, \frac{\pi}{2}$)
λ	Ecliptic longitude	Uniform($0, 2\pi$)
t_c	Coalescence time (day)	Uniform($3, 365.25$)
ϕ_c	Reference phase	Uniform($0, 2\pi$)
ψ	Polarization angle	Uniform($0, \pi$)
(s_{1z}, s_{2z})	z components of the binary's dimensionless spins	Uniform($-0.9, 0.9$)

TABLE I. Priors of parameters (z -axis is parallel to the orbital angular momentum).

uniform distributions listed in Tab. I. The observation time of LISA is considered to be 1 year.

The Gaussian instrumental noise used here is generated from the PSD of LISA noise, which is based on the LISA Science Requirement Document [35, 36]. According to the document, the acceleration noise S_{acc} and the displacement noise S_{OMS} are given by

$$S_{\text{acc}}^{1/2} = 3 \frac{\text{fm} \cdot \text{s}^{-2}}{\sqrt{\text{Hz}}} \sqrt{1 + \left(\frac{0.4 \text{ mHz}}{f}\right)^2} \sqrt{1 + \left(\frac{f}{8 \text{ mHz}}\right)^4},$$

$$S_{\text{OMS}}^{1/2} = 15 \frac{\text{pm}}{\sqrt{\text{Hz}}} \sqrt{1 + \left(\frac{2 \text{ mHz}}{f}\right)^4}. \quad (4)$$

The LISA Data Challenge (LDC) group [36] has generated 1-year LISA data that contains simulated waveforms from 30 million Galactic white dwarf binaries. For the training data, this kind of GW signals are treated as background noise, although some of them are detectable individually. We also simulate the background noise produced by Galactic binaries from the PSD that is estimated from the LDC data. The noise generated in this way is Gaussian and stationary, although in fact the galactic signals should be treated as the non-Gaussian and non-stationary noises modulated by the distribution of the sources in the Milky Way [37, 38].

For LISA, the TDI technique is applied to suppress the laser frequency noise [39–45]. We choose the uncorrelated TDI observables A and E [41] as two channels of the data passed through our neural network, as showed in Fig. 1. We generated training data using TDI-1.0 [46] with LDC's codes provided in challenge-1 (LDC-1) [47].

We set the input size of MFCNN as 16,384 and the sampling rate as 1/15 Hz. For the templates used in the first layer of the MFCNN, we take equal-mass MBHB sources at $z = 3$ and sample the logarithm of M_z evenly in the range of ($10^{5.4} M_\odot, 10^8 M_\odot$). The number of templates is set to 50. We generate five datasets with $z = 1, 3, 6, 10, 15$, and the MFCNN model is trained on each dataset independently. The training process is done within 10 hours on a NVIDIA GeForce RTX 2080 GPU with 8GB of memory.

V. RESULTS

A. Generalization test

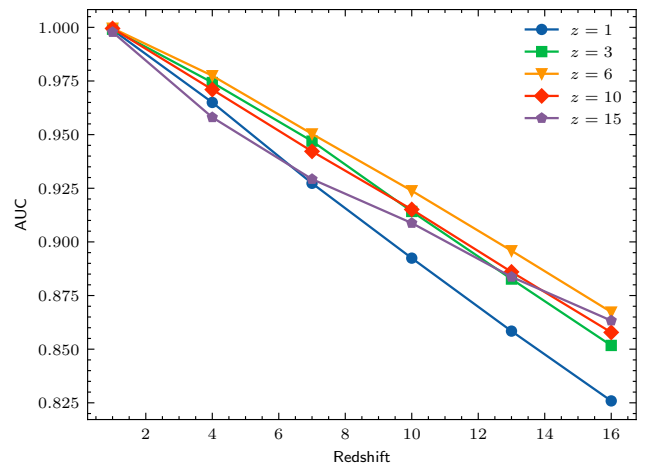


FIG. 2. AUC of the MFCNN models as a function of redshifts. The testing datasets are generated by IMRPhenomD model. The colored lines denote the five MFCNN models trained on datasets with $z = 1, 3, 6, 10, 15$, respectively.

In this section, we employ the receiver operating characteristics (ROC) analysis [48, 49] to visualize the performance of the MFCNN model in testing stage. The ROC curve is a graphical plot that depicts the true positive rate (TPR) and false positive rate (FPR) [49] as the discrimination threshold is varied. To compare classifier performance, the area under the ROC curve (AUC) [49–51] has long been used to quantify the ROC performance, which is a single scalar value varying between 0 and 1. The AUC is a threshold-free metric capable of measuring the overall performance of binary classifiers. The closer the AUC to 1, the better the classifier.

Firstly, we test the MFCNN model on the datasets which assume independently identically distributed about the training set. Each testing dataset with various redshift z contains 3,000 positive samples (with MBHB signals) and 3,000 negative samples (without MBHB signals). We generate waveforms of MBHB signals using the IMRPhenomD model, which is the same as training. The priors are the same as Tab. I. We shift the grid of

M_z and q from the values in training data. Therefore, every test sample does not appear in the learning process. We show the performances on testing datasets with various redshifts in Fig. 2. Our MFCNN model attains optimal performance in AUC as we shift the redshift between $z = 1$ and $z = 16$ for testing while the model trained on $z = 6$ achieve best practice among the others. Here we will use this model for the following test. In Fig. 3, we also vary the threshold of prediction from 0 to 1 to show the ROC curves for each test dataset. As we vary the observing limit from $z = 1$ to $z = 16$ for $\text{FPR} = 10^{-3}$ while the TPR decrease from 0.997 to 0.627. Our model achieves a high level of sensitivity and is capable to capture the distinctive waveform features of MBHBs in highly noisy environments.

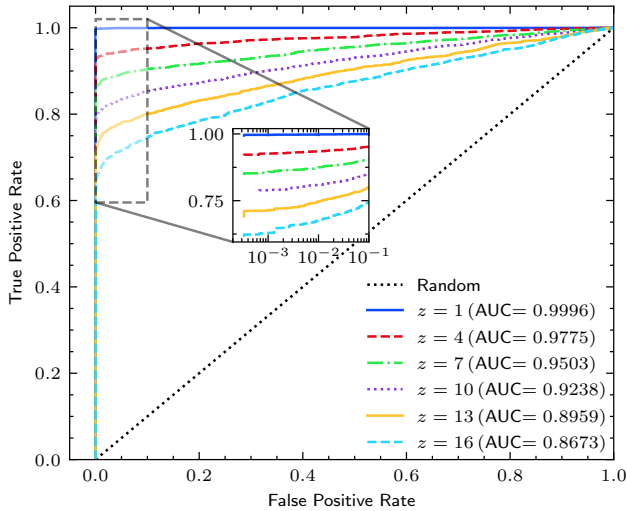


FIG. 3. ROC analysis for the MFCNN model trained with $z = 6$. The redshifts of the testing datasets are selected to be 1, 4, 7, 10, 13, 16. The black dotted line denotes the line of random classifier. The grey dashed box indicates the region of the inset.

In reality, MBHB signals have richer features than the approximate waveform template. The IMRPhenomD waveform only considers the aligned-spin black hole binaries with circular orbits. However, more complicated evolution of MBHBs in LISA band should be considered, such as residual eccentricity [52] and precession of binary’s orbital plane [53–55]. The waveform will be modulated due to these facts. It is necessary for the neural network to work well on the MBHB waveforms beyond the training dataset. Thus, we further test the generalization ability of the MFCNN model on other different waveform family.

We generate new datasets by SEOBNRv4 [56], SENBNRE [57–59] and SEOBNRv4P [60–62] models. The SEOBNRv4 model deals with the same binary system as IMRPhenomD, but they are different in implementation of modeling. The SEOBNRE model can simulate the GW waveforms of eccentric MBHBs and we

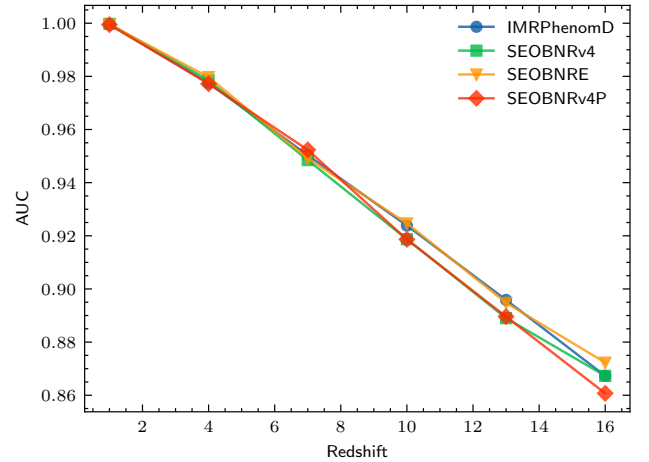


FIG. 4. Performance of the MFCNN model on different waveform families. The testing datasets are generated by IMRPhenomD, SEOBNRv4, SEOBNRE and SEOBNRv4P.

sample the parameter of eccentricity uniformly in the range of $(0, 0.3)$. The SEOBNRv4P model captures the precession-modulated waveforms, in which the spins of binary system are characterized by (s_{1x}, s_{1y}, s_{1z}) and (s_{2x}, s_{2y}, s_{2z}) . We sample them uniformly in the range of $(-0.9, 0.9)$. Note that s_{1i} and s_{2i} are components of the binary’s dimensionless spins along three coordinate axes. The z-axis is parallel to the initial orbital angular momentum. The x-axis is parallel to the line of two black holes at initial state and the y-axis is perpendicular to the other two axes. Further constraints are set with Kerr limit

$$s_{1x}^2 + s_{1y}^2 + s_{1z}^2 \leq 1, \quad s_{2x}^2 + s_{2y}^2 + s_{2z}^2 \leq 1. \quad (5)$$

We test the MFCNN model on the datasets generated by four different waveform family as shown in Fig. 4. Compared to the IMRPhenomD waveform we used for training, the performances of the model on the modulated waveform families are very similarly.

It turned out that our model has a nice ability of robust extrapolation outside the representations of our training region. This implies that for real LISA data in the future, our model may have the power to search for the signals beyond the theoretical templates.

B. Sangria dataset

To handle more realistic data, we use Sangria dataset from LDC-2 [36] to demonstrate the performance of trigger generation with our MFCNN model. The dataset covers a roughly 1-year LISA data and contains the simulated waveforms from 30 million Galactic binaries, 17 verification Galactic binaries and 15 coalescing MBHBs. We downsample it to 1/15 Hz for consistency. Then, it is divided into overlapping segments corresponding to the in-

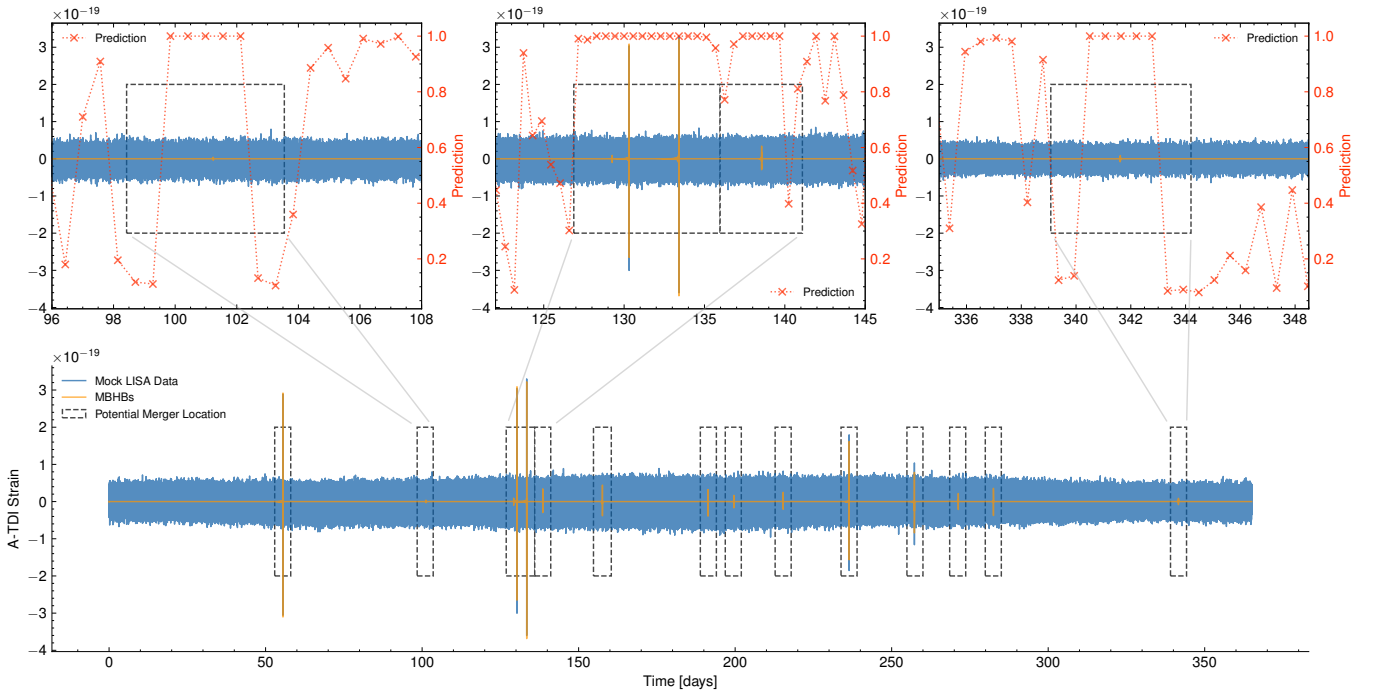


FIG. 5. Prediction of the MFCNN model on 1-year LISA data simulated by the LDC group. The blue line is the A-TDI data, the orange line denotes the 15 MBHB signals which are clearly visible and the dashed boxes denote the range of coalescence time predicted by our model. Three zoomed regions are shown in upper panel. The red cross indicates the prediction from the MFCNN model.

put size of our model, as we discussed in Sec. III. And let all the segments pass through the MFCNN model resulting a sequence of predictions for further analysis. Based on our search strategy in Sec. III, the local-maximum triggers resulted are recognized as containing MBHB coalescence. We output the center time of the segments with potential merger location. It takes only ten seconds for a model to analyze the 1-year data on our device. The result of the model trained on $z = 6$ is shown in Fig. 5. It shows that all 15 MBHB mergers are located within a short segment. Particularly, on the upper left and upper right panel of Fig. 5, both of the two MBHB signals with the smallest amplitude and the furthest distance can be clearly recognized by our MFCNN model. Each trigger implies that the range of coalescence time is 5.12 days. The target MBHB mergers are just right in the middle. We find that this is always the case. Note that we can also achieve the desired output even when multiple MBHBs merger that are close together. Examples for this are shown in upper middle panel of Fig. 5.

Note that the MFCNN model is trained on datasets with the Gaussian and stationary noise. The GW signals from Galactic binaries in LDC's 1-year data generally are regard as non-Gaussian and non-stationary noise [38]. Furthermore, we use the code in LDC-1 [47] to generate the TDI-1.0 response in our training process (Sec. IV). In LDC-2, a different code named LISANode [63] is used to produce the TDI-1.5 response for the Sangria dataset [64].

Although the differences of code and TDI generation are beyond the range of train data, our model still has the ability to recognize all MBHBs and report no false alarms. It implies that the MFCNN model shows a robust resistance on dynamic modulation of space-based GW detectors and captures the general representations of the waveform response. This shows that our model is expected to perform well on real LISA data.

VI. SUMMARY

We have demonstrated that deep learning, when applied to LISA data, are capable to search for MBHB coalescences. We employ the MFCNN with a small amount of templates and produce output on 1-year Sangria LISA dataset within ten seconds. The model can identify all 15 MBHB mergers with no false alarms and each of them is reported for data segments as short as 5.12-days. These results lay the foundation for accelerating the detection and forecasting the mergers of MBHBs that can provide early warnings to enable the observation of electromagnetic counterparts. By building a neural network that is capable of rapidly searching for and counting MBHBs we answer a fundamental question regarding the applicability of neural networks for the LISA data analysis.

In this work, we have showed a nice robust resistance for numerous GW sources and modulation of waveform family. This generation ability of the supervised learning

approach can also be extended to varying data simulation methods and updated generations of TDI, which presents an effective tool for further analysis. It is also suitable to other space-based GW detectors.

ACKNOWLEDGMENTS

We thank Zhoujian Cao for his helpful comments and discussions. CL would like to thank Stanislav Babak for help in the use of the LDC code and datasets. WHR would like to thank Pengfei Zhou for discussion on CNN. We thank the Peng Cheng Nation Laboratory (PCNL)

Cloud Brain for computation support. This work is supported in part by the National Key Research and Development Program of China Grant No. 2020YFC2201501, in part by the National Natural Science Foundation of China under Grant No. 12075297 and No. 11690021.

The authors would like to acknowledge the work of the LDC group. For this study, both the LDC software and datasets were used [36]. PyCBC [65] and LALSuite [66] are also used to generate gravitational strains of coalescing MBHBs. Plots are generated by Matplotlib [67, 68]. The implementation of the MFCNN model is coded based on PyTorch [69].

-
- [1] B. P. Abbott *et al.* (LIGO Scientific, Virgo), *Phys. Rev. Lett.* **116**, 061102 (2016), [arXiv:1602.03837 \[gr-qc\]](#).
- [2] B. Abbott, R. Abbott, T. Abbott, S. Abraham, F. Acernese, K. Ackley, C. Adams, R. Adhikari, V. Adya, C. Affeldt, *et al.*, *Physical Review X* **9**, 031040 (2019).
- [3] R. Abbott, T. Abbott, S. Abraham, F. Acernese, K. Ackley, A. Adams, C. Adams, R. Adhikari, V. Adya, C. Affeldt, *et al.*, *Physical Review X* **11**, 021053 (2021).
- [4] R. Abbott *et al.* (LIGO Scientific, VIRGO, KAGRA), (2021), [arXiv:2111.03606 \[gr-qc\]](#).
- [5] J. Kormendy and D. Richstone, *Ann. Rev. Astron. Astrophys.* **33**, 581 (1995).
- [6] J. Magorrian *et al.*, *Astron. J.* **115**, 2285 (1998), [arXiv:astro-ph/9708072](#).
- [7] M. C. Begelman, R. D. Blandford, and M. J. Rees, *Nature* **287**, 307 (1980).
- [8] P. Amaro-Seoane *et al.* (LISA), (2017), [arXiv:1702.00786 \[astro-ph.IM\]](#).
- [9] D. E. Holz and S. A. Hughes, *Astrophys. J.* **629**, 15 (2005), [arXiv:astro-ph/0504616](#).
- [10] K. Kyutoku and N. Seto, *Phys. Rev. D* **95**, 083525 (2017), [arXiv:1609.07142 \[astro-ph.CO\]](#).
- [11] T. Robson and N. Cornish, *Class. Quant. Grav.* **34**, 244002 (2017), [arXiv:1705.09421 \[gr-qc\]](#).
- [12] N. J. Cornish and J. Crowder, *Phys. Rev. D* **72**, 043005 (2005), [arXiv:gr-qc/0506059](#).
- [13] Y. LeCun, Y. Bengio, and G. Hinton, *nature* **521**, 436 (2015).
- [14] E. Cuoco, J. Powell, M. Cavaglià, K. Ackley, M. Berger, C. Chatterjee, M. Coughlin, S. Coughlin, P. Easter, R. Essick, *et al.*, *Machine Learning: Science and Technology* **2**, 011002 (2020).
- [15] L. J. Rubbo, N. J. Cornish, and O. Poujade, *Phys. Rev. D* **69**, 082003 (2004), [arXiv:gr-qc/0311069](#).
- [16] M. Tinto and S. V. Dhurandhar, *Living Reviews in Relativity* **24**, 1 (2021), [arXiv:gr-qc/0409034 \[gr-qc\]](#).
- [17] H. Wang, S. Wu, Z. Cao, X. Liu, and J.-Y. Zhu, *Phys. Rev. D* **101**, 104003 (2020), [arXiv:1909.13442 \[astro-ph.IM\]](#).
- [18] B. J. Owen and B. S. Sathyaprakash, *Phys. Rev. D* **60**, 022002 (1999), [arXiv:gr-qc/9808076](#).
- [19] Y. LeCun, L. Bottou, Y. Bengio, and P. Haffner, *Proceedings of the IEEE* **86**, 2278 (1998).
- [20] B. P. Abbott *et al.* (LIGO Scientific, Virgo), *Phys. Rev. D* **93**, 122003 (2016), [arXiv:1602.03839 \[gr-qc\]](#).
- [21] H. Gabbard, M. Williams, F. Hayes, and C. Messenger, *Phys. Rev. Lett.* **120**, 141103 (2018), [arXiv:1712.06041 \[astro-ph.IM\]](#).
- [22] D. George and E. A. Huerta, *Phys. Rev. D* **97**, 044039 (2018), [arXiv:1701.00008 \[astro-ph.IM\]](#).
- [23] D. George and E. A. Huerta, *Phys. Lett. B* **778**, 64 (2018), [arXiv:1711.03121 \[gr-qc\]](#).
- [24] T. D. Gebhard, N. Kilbertus, I. Harry, and B. Schölkopf, *Physical Review D* **100**, 063015 (2019).
- [25] P. G. Krastev, *Physics Letters B* **803**, 135330 (2020).
- [26] M. B. Schäfer, F. Ohme, and A. H. Nitz, *Physical Review D* **102**, 063015 (2020).
- [27] H. Xia, L. Shao, J. Zhao, and Z. Cao, *Physical Review D* **103**, 024040 (2021).
- [28] W.-H. Ruan, Z.-K. Guo, R.-G. Cai, and Y.-Z. Zhang, *Int. J. Mod. Phys. A* **35**, 2050075 (2020), [arXiv:1807.09495 \[gr-qc\]](#).
- [29] B. Allen, W. G. Anderson, P. R. Brady, D. A. Brown, and J. D. E. Creighton, *Phys. Rev. D* **85**, 122006 (2012), [arXiv:gr-qc/0509116](#).
- [30] E. Huerta, A. Khan, X. Huang, M. Tian, M. Levental, R. Chard, W. Wei, M. Hefin, D. S. Katz, V. Kondratenko, *et al.*, *Nature Astronomy* **5**, 1062 (2021).
- [31] W. Wei, A. Khan, E. Huerta, X. Huang, and M. Tian, *Physics Letters B* **812**, 136029 (2021).
- [32] S. A. Usman, A. H. Nitz, I. W. Harry, C. M. Biwer, D. A. Brown, M. Cabero, C. D. Capano, T. Dal Canton, T. Dent, S. Fairhurst, *et al.*, *Classical and Quantum Gravity* **33**, 215004 (2016).
- [33] S. Husa, S. Khan, M. Hannam, M. Pürrer, F. Ohme, X. Jiménez Forteza, and A. Bohé, *Phys. Rev. D* **93**, 044006 (2016), [arXiv:1508.07250 \[gr-qc\]](#).
- [34] S. Khan, S. Husa, M. Hannam, F. Ohme, M. Pürrer, X. Jiménez Forteza, and A. Bohé, *Phys. Rev. D* **93**, 044007 (2016), [arXiv:1508.07253 \[gr-qc\]](#).
- [35] The LISA Science Study Team, “ESA-L3-EST-SCI-RS-001,” <https://atrium.in2p3.fr/f5a78d3e-9e19-47a5-aa11-51c81d370f5f> (2018).
- [36] LISA Consortium’s LDC working group, “LISA Data Challenges,” <https://lisa-ldc.lal.in2p3.fr> (2019).
- [37] M. R. Adams and N. J. Cornish, *Phys. Rev. D* **82**, 022002 (2010), [arXiv:1002.1291 \[gr-qc\]](#).
- [38] N. J. Cornish, (2021), [arXiv:2110.06238 \[gr-qc\]](#).
- [39] S. V. Dhurandhar, K. Rajesh Nayak, and J. Y. Vinet, *Phys. Rev. D* **65**, 102002 (2002), [arXiv:gr-qc/0112059](#).

- [40] M. Tinto, F. B. Estabrook, and J. W. Armstrong, *Phys. Rev. D* **65**, 082003 (2002).
- [41] T. A. Prince, M. Tinto, S. L. Larson, and J. W. Armstrong, *Phys. Rev. D* **66**, 122002 (2002), [arXiv:gr-qc/0209039](#).
- [42] M. Tinto, D. A. Shaddock, J. Sylvestre, and J. W. Armstrong, *Phys. Rev. D* **67**, 122003 (2003), [arXiv:gr-qc/0303013](#).
- [43] D. A. Shaddock, M. Tinto, F. B. Estabrook, and J. W. Armstrong, *Phys. Rev. D* **68**, 061303 (2003), [arXiv:gr-qc/0307080](#).
- [44] M. Tinto, F. B. Estabrook, and J. W. Armstrong, *Phys. Rev. D* **69**, 082001 (2004), [arXiv:gr-qc/0310017](#).
- [45] N. J. Cornish and R. W. Hellings, *Class. Quant. Grav.* **20**, 4851 (2003), [arXiv:gr-qc/0306096](#).
- [46] M. Vallisneri, *Phys. Rev. D* **71**, 022001 (2005), [arXiv:gr-qc/0407102](#).
- [47] S. Babak and A. Petiteau, “LISA Data Challenge Manual,” <https://lisa-ldc.lal.in2p3.fr/static/data/pdf/LDC-manual-002.pdf> (2018).
- [48] J. P. Egan and J. P. Egan, *Signal detection theory and ROC-analysis* (Academic press, 1975).
- [49] T. Fawcett, *Pattern recognition letters* **27**, 861 (2006).
- [50] A. P. Bradley, *Pattern recognition* **30**, 1145 (1997).
- [51] J. A. Hanley and B. J. McNeil, *Radiology* **143**, 29 (1982).
- [52] A. Sesana, *Astrophys. J.* **719**, 851 (2010), [arXiv:1006.0730 \[astro-ph.CO\]](#).
- [53] C. Cutler *et al.*, *Phys. Rev. Lett.* **70**, 2984 (1993), [arXiv:astro-ph/9208005](#).
- [54] T. A. Apostolatos, C. Cutler, G. J. Sussman, and K. S. Thorne, *Phys. Rev. D* **49**, 6274 (1994).
- [55] A. Vecchio, *Phys. Rev. D* **70**, 042001 (2004), [arXiv:astro-ph/0304051](#).
- [56] A. Bohé *et al.*, *Phys. Rev. D* **95**, 044028 (2017), [arXiv:1611.03703 \[gr-qc\]](#).
- [57] Z. Cao and W.-B. Han, *Phys. Rev. D* **96**, 044028 (2017), [arXiv:1708.00166 \[gr-qc\]](#).
- [58] X. Liu, Z. Cao, and L. Shao, *Phys. Rev. D* **101**, 044049 (2020), [arXiv:1910.00784 \[gr-qc\]](#).
- [59] X. Liu, Z. Cao, and Z.-H. Zhu, (2021), [arXiv:2102.08614 \[gr-qc\]](#).
- [60] Y. Pan, A. Buonanno, A. Taracchini, L. E. Kidder, A. H. Mroué, H. P. Pfeiffer, M. A. Scheel, and B. Szilágyi, *Phys. Rev. D* **89**, 084006 (2014), [arXiv:1307.6232 \[gr-qc\]](#).
- [61] S. Babak, A. Taracchini, and A. Buonanno, *Phys. Rev. D* **95**, 024010 (2017), [arXiv:1607.05661 \[gr-qc\]](#).
- [62] S. Ossokine *et al.*, *Phys. Rev. D* **102**, 044055 (2020), [arXiv:2004.09442 \[gr-qc\]](#).
- [63] J.-B. Bayle, M. Lilley, A. Petiteau, and H. Halloin, *Phys. Rev. D* **99**, 084023 (2019), [arXiv:1811.01575 \[astro-ph.IM\]](#).
- [64] S. Babak, M. Le Jeune, A. Petiteau, and M. Vallisneri, “LISA Data Challenge: Sangria,” <https://lisa-ldc.lal.in2p3.fr/static/data/pdf/LDC-manual-Sangria.pdf> (2020).
- [65] A. Nitz, I. Harry, D. Brown, C. M. Biwer, J. Willis, T. D. Canton, C. Capano, T. Dent, L. Pekowsky, A. R. Williamson, G. S. C. Davies, S. De, M. Cabero, B. Machenschalk, P. Kumar, D. Macleod, S. Reyes, dfinstad, F. Panmarale, T. Massinger, S. Kumar, M. Tápai, L. Singer, S. Khan, S. Fairhurst, A. Nielsen, S. Singh, K. Chandra, shasvath, and B. U. V. Gadre, “*gwastro/pycbc*,” (2021).
- [66] LIGO Scientific Collaboration, “*LIGO Algorithm Library - LALSuite*,” free software (GPL) (2018).
- [67] J. D. Hunter, *Computing in Science & Engineering* **9**, 90 (2007).
- [68] T. A. Caswell, M. Droettboom, A. Lee, E. S. de Andrade, T. Hoffmann, J. Hunter, J. Klymak, E. Firing, D. Stansby, N. Varoquaux, J. H. Nielsen, B. Root, R. May, P. Elson, J. K. Seppänen, D. Dale, J.-J. Lee, D. McDougall, A. Straw, P. Hobson, hannah, C. Gohlke, T. S. Yu, E. Ma, A. F. Vincent, S. Silvester, C. Moad, N. Kniazev, E. Ernest, and P. Ivanov, “*matplotlib/matplotlib: Rel: v3.4.3*,” (2021).
- [69] A. Paszke, S. Gross, F. Massa, A. Lerer, J. Bradbury, G. Chanan, T. Killeen, Z. Lin, N. Gimelshein, L. Antiga, A. Desmaison, A. Kopf, E. Yang, Z. DeVito, M. Raison, A. Tejani, S. Chilamkurthy, B. Steiner, L. Fang, J. Bai, and S. Chintala, in *Advances in Neural Information Processing Systems 32*, edited by H. Wallach, H. Larochelle, A. Beygelzimer, F. d'Alché-Buc, E. Fox, and R. Garnett (Curran Associates, Inc., 2019) pp. 8024–8035.